Fine-Tuning the Surface and Interfacial Chemistry of Silica Nanoparticles to Control Stability in High Ionic Strength Electrolytes and Modulate Assembly at Oil−Water Interfaces

Published as part of Chemistry of Materials virtual special issue "In Honor of Prof. Clement Sanchez".

Ahmed Wasel Alsmaeil, Sohaib Mohammed, Bashayer Saad Aldakkan, Nikolaos Chalmpes, Antonios Kouloumpis, Georgia Potsi, Andrew Galvin, Greeshma Gadikota, Mazen Yousef Kanj, and Emmanuel P. Giannelis*

Cite This: https://doi.org/10.1021/acs.chemmater.3c01871

Read Online

ACCESS | Metrics & More | Article Recommendations | Supporting Information

ABSTRACT: Controlling the interfacial chemistry is critical to the behavior of several material systems. In this report, we demonstrate how subtle changes in the surface chemistry of silica nanoparticles have a profound effect on their colloidal stability, as well as their ability to assemble at oil−water interfaces. The ability to direct the assembly by fine-tuning the surface chemistry of nanoparticles, NPs, allows for controlling the interfacial properties and the overall behavior of the resulting Pickering emulsions. We start by showing that the colloidal stability of silica nanoparticles functionalized by a mixture of silanes is dramatically improved compared to that of silica functionalized with either one. For example, NP suspensions synthesized using a 50:50 mixture of N1-(3-trimethoxysilylpropyl)diethylenetriamine and N-trimethoxysilylpropyl-N,N,N-trimethylammonium in a complex brine containing a mixture of salts remain suspended when subjected to acceleration of 500 × $\vec{g}$ and temperatures as high as 60 °C. In contrast, particles functionalized with either one of the silanes are far less stable under the same conditions. The colloidal stability of the particles is correlated to the silane-grafted layers and surface roughness obtained by atomic force microscopy (AFM). We next studied the mechanism of the particles' assembly at oil−water interfaces and characterized the interfacial properties under various conditions. In all cases, the assembly is driven by electrostatic interactions between the positively charged particles and the negatively charged oil surface. Ultrasmall-/small-angle X-ray scattering measurements confirm the assembly of nanoparticles at the interface, and time-dependent scattering measurements reveal the presence of two steps in the assembly in brine, consistent with the interfacial tension dynamics. The assembled particles at the interface lead to a solid-like behavior or jamming, with the interface behaving like an elastic membrane with high dilatational and storage moduli. This study provides fundamental insights into the surface and interfacial properties of silane-grafted NPs and ways to fine-tune their assembly at oil−water interfaces while improving their colloidal stability under harsh environmental conditions.
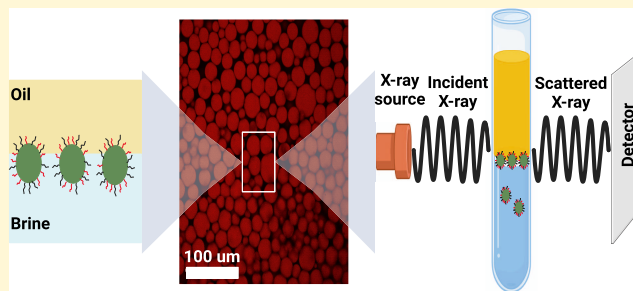
INTRODUCTION

Surface functionalization of nanoparticles, including silica nanoparticles, is a necessary step to fine-tune their inter- and intramolecular interactions and thus their behavior. A common approach is based on using different types of silanes, which are reacted with the particles via surface hydroxyl groups.[1−5] The grafted silanes endow the particles with distinct surface chemistry and properties. While there is ample information regarding surface modification using single silanes,[6−10] the literature appears sparse, when more than one silane is used concurrently for functionalization.[11,12]

Manipulating the properties of liquid−liquid interfaces and specifically oil−water interfaces using nanoparticles (so-called Pickering emulsions) has attracted widespread attention due to both scientific interest as well as use in practical applica-

tions.[13−23] Assembly of nanoparticles of various chemistries and dimensionalities at the oil−water interfaces stabilizes the emulsion and offers the possibility to synthesize materials with controlled behavior by fine-tuning interfacial properties.[18,24,25] By varying the chemistry and dimensionality of the nanoparticles, the adsorption energy and thus the interfacial properties can be modulated and controlled.[18,26]

A

Nanoparticle assembly and thus interfacial properties can be fine-tuned by controlling the pH,[27−29] electric and magnetic fields,[30−32] or combinations thereof.[33] Previous reports have emphasized the effect of charge screening on particle assembly in the presence of electrolytes. Adding ions to the medium screens surface charges, which suppresses particle−particle repulsion and improves the packing density of the particles at the interface.[34,35] For instance, the assembly of silica NPs functionalized with carboxylic acid groups varies with NaCl concentration. The equilibrium interfacial tension (IFT) decreased from approximately 29 mN/m in the ion-free suspension to 20 mN/m with 500 mM NaCl. With increasing ion concentration, the interface transformed from liquid-like to solid-like due to the dense packing of NPs at the interface.[36] However, there is a trade-off since the presence of ions and the associated screening of the surface charges decrease the colloidal stability of the suspension.[37−40]

We previously reported the assembly of positively charged silica NPs at oil−water interfaces modified by two silanes but did not provide detailed information on their surface chemistry or colloidal behavior. In addition, we did not compare the double silane-functionalized NPs to those synthesized by either silane.[41] In this paper, we use a number of analytical techniques, including atomic force microscopy (AFM) and transmission electron microscopy (TEM) to characterize in detail the surface chemistry and morphology of the double silane-functionalized NPs and contrast to those functionalized by either one. We also show that the double silane-functionalized NPs exhibit enhanced colloidal stability, especially in the presence of various electrolytes. Using the colloidally stable silica NPs, we study the assembly mechanism at oil−water interfaces using static- and time-dependent measurements, including in operando ultrasmall-/small-angle X-ray scattering (USAXS/SAXS).[16,17] We finally relate the mechanistic information to the interfacial mechanical properties in tension as well as in shear. We find that when the particles are dispersed in brine, the assembly becomes solid-like with a behavior similar to an elastic film. The fundamental insights provided by this study can serve as a base for understanding the surface and interfacial properties of NPs in general and silica in particular. Furthermore, this strategy can be exploited to improve colloidal stability under harsh environmental conditions (both salinity and temperature) as well as fine-tune their assembly at oil−water interfaces to control the properties of the resulting Pickering emulsions.

EXPERIMENTAL SECTION

Materials. Colloidal silica NPs (LUDOX, 30 wt % in water) with an average diameter of 12 nm, hydrochloric acid (37 wt %), N1-(3-trimethoxysilylpropyl) diethylenetriamine (TMPA), sodium chloride (NaCl), calcium chloride dihydrate (CaCl$_2$·2H$_2$O), magnesium chloride hexahydrate (MgCl$_2$·6H$_2$O), sodium sulfate (Na$_2$SO$_4$), sodium bicarbonate (NaHCO$_3$), hexadecane, and stearic acid were all purchased from Sigma-Aldrich and used without further purification. N-trimethoxysilylpropyl-N,N,N-trimethylammonium chloride (TMAC), 50% in methanol, was obtained from Gelest. Crude oil (density 0.82 g/mL and viscosity 6.1 mPa·s) was obtained from the Cornell Energy Systems Institute. The composition of the crude oil determined by SARA analysis (saturates, aromatics, resins, and asphaltene) is 33.1% saturates, 47.3% aromatics, 8.7% resins (polar I), and 10.9% asphaltenes (polar II). The complex brine is made by dissolving the appropriate amount of salt to make a final solution composed of 701 mM NaCl, 22 mM CaCl$_2$, 185 mM MgCl$_2$, 44 mM Na$_2$SO$_4$, and 1.6 mM NaHCO$_3$. In some experiments, model oil was used, which is prepared by dissolving 10 mM stearic acid in hexadecane.

Surface Functionalization of the Silica NPs. As we reported previously, the SiO$_2$ NPs were surface-modified using a 1:1 mixture of TMPA and TMAC. Briefly, in 30 mL of deionized water (DIW), 3 g of TMAC and 1.5 g of TMPA (pH 10) were mixed by stirring vigorously at room temperature for 30 min. In parallel, 9 g of silica NPs was ultrasonicated for 30 min at 30% amplitude in an ice bath to minimize heating of the suspension. After that, the particles were added to 150 mL of DI water in a 200 mL round-bottom flask and sonicated for an additional 1 h. The TMAC and TMPA mixture was then added dropwise to the silica suspension while being sonicated. The color of the suspension immediately changed from clear to white. After that, the reaction mixture was transferred to an oil bath and kept stirring at 70 °C overnight. The pH of the reaction was 9.5 and remained unchanged throughout the synthesis. The product (referred to as $S_{1,2}$) was collected and dialyzed against water for 7 days. The water in the dialysis apparatus was changed twice a day and the pH was kept at 4−5 by adding aliquots of 0.1 M HCl or 0.1 M NaOH.[41] Synthesis of single-functionalized silica NPs was carried out using a similar procedure except that either 6 g of TMAC or 3 g of TMPA was added to 9 g of LUDOX particles to synthesize the S_1 or S_2 suspension, respectively. The pH of the synthesis of S_1 was 7.5 while that of S_2 was 10.5.

Methods. Transmission electron microscopy (TEM) was also used to investigate the morphology and size of the particles. The imaging was conducted using an LaB6 electron source at 120 kV and a Gatan Orius S1000 CCD camera on an FEI-Tecnai 12 BioTwin TEM from FEI Co., Hillsboro, OR. Prior to imaging, 1 wt % suspension of the particles in water was cast on a carbon-coated copper grid. The particle size distribution was then analyzed by using ImageJ.

Surface functionalization of the particles was confirmed by X-ray photoelectron spectroscopy (XPS) (ScientaOmicron ESCA 2SR XPS). The instrument was equipped with an AI Kα 1486.7 eV monochromator that operated at a pressure of 10^{-9} Torr. The sample, in powder form, was deposited on copper tape. Surveys were collected at 200 eV pass energy, and high-resolution scans were collected at 50 eV. All of the binding energies were referenced to the C 1s core level region.

ζ-potential was determined using a Zetasizer (ZS90, Malvern Instruments) at 25 °C and a backscattering detection angle of 173°. 1 wt % suspension of silica and 10 vol % of oil-in-water emulsions in Malvern polycarbonate folded capillary cells (DTS1070) were used. The emulsion was prepared using a Fisher Scientific Q500 ultrasonicator at 10% amplitude for 10 min while the pH of the aqueous phase was adjusted to 7 using 0.1 M NaOH. For the measurements of the ζ-potential in brine, a Malvern Universal Dip Cell (ZEN 1002) was used with the suspension in a cuvette (PCS 1115) to minimize corrosion to the electrodes because of the high salinity brine. Different brine concentrations were prepared by diluting the initial brine with DI water.

Colloidal stability was assessed using a STEP-Technology LUMiSizer 651 (LUM, Gmbh, Germany). In this technique, the suspension placed in 10 mm polyamide (PA) is centrifuged at an acceleration of 500 × $\vec{g}$ and temperatures from 25 to 60 °C while transmission at 410 nm is followed through a vial with time. Stability was determined by monitoring the transmission profiles, and the separation indices were calculated using SEPView software (LUM, Gmbh, Germany). The separation index is evaluated from the transmission of the system at a certain time (T_i) subtracted from the first transmission profile (T_1) and divided by the maximum transmission through the vial. For stable suspensions, the transmission remains constant with time ($T_1 = T_i$) and the separation index is 0. On the other hand, for suspensions where aggregation and sedimentation do take place, the transmission decreases and the separation index increases with time. A separation index of 1 corresponds to complete particle sedimentation.[42]

To gain further insights on how the different particle suspensions behave in various electrolytes, quartz crystal microbalance, QCM,
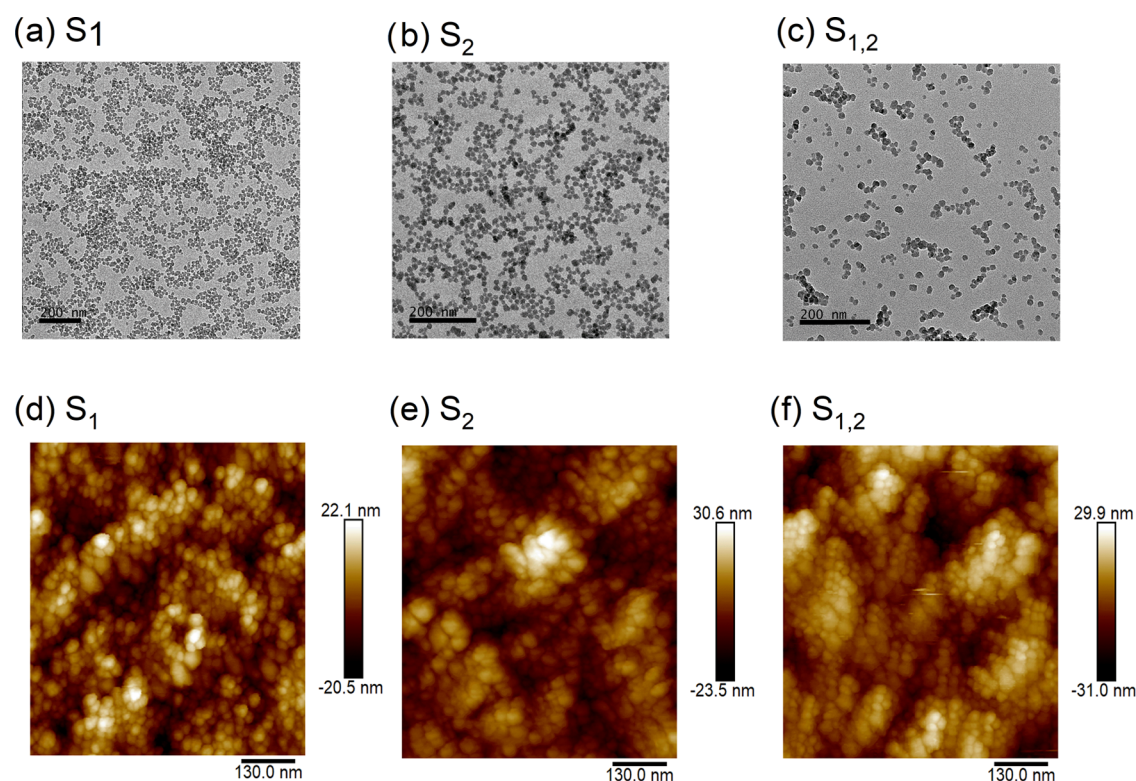
Figure 1. TEM images of different NPs (top panels): S_1 (a), S_2 (b), and $S_{1,2}$ (c). AFM images taken in a liquid cell in the presence of DI water (bottom panels): S_1 (d), S_2 (e), and $S_{1,2}$ (f).

experiments were conducted using a Qsense E1 (Biolin Scientific, Sweden). A Au sensor (QSX 301, Biolin Scientific) was cleaned according to the supplier's protocol prior to each measurement. Briefly, the sensor was UV-treated for 10 min. A 5:1:1 mixture of DI water, ammonia (25%), and hydrogen peroxide (30%) was heated to 75 °C and the sensor was placed in the solution for 5 min. The sensor was then rinsed with DI water, followed by drying with nitrogen gas and treated with UV again for 10 min. After that, 1 wt % of the suspension was drop-cast on the sensor and allowed to dry overnight. DI water was then injected at a flow rate of 0.3 mL/min to establish a baseline. After that, the complex brine mixture was injected for 30 min at 0.3 mL/min, followed by rinsing with DI water at the same flow rate. To the first approximation, the mass of brine adsorbed on the surface is related to the change of frequency according to the Sauerbrey equation[43]

$$\Delta m = -\frac{C\Delta f}{n} \tag{1}$$

where Δm is the adsorbed mass, n is the overtone number (3rd in this experiment), and C is the constant indicative of the device sensitivity, which is 1.8 ng/cm^2 for the crystal with a fundamental resonance frequency of 5 MHz.

A spinning drop tensiometer (SDT, KRÜSS) was used to determine the interfacial tension, IFT, and dilatational modulus. An oil droplet was released in a capillary tube with an inner diameter of 3.25 mm that was prefilled with water or a suspension of the NPs. The shape of the droplet was fitted using the Young–Laplace equation, and the IFT was determined using ADVANCE software (KRÜSS). When the IFT reached an equilibrium value, the oil droplet was sinusoidally dilated using 1000 rpm amplitude and 0.1 Hz to determine the dilatational modulus of the interfacial layer. The variation of the surface area and IFT was recorded, and the following equation was used to determine the complex dilatational modulus[44−46]

$$E = A\frac{\partial \gamma}{\partial A} \tag{2}$$

where γ is the interfacial tension and A is the surface area of the oil droplet.

Interfacial rheology was measured with a Discovery Hybrid Rheometer (DHR3, TA Instruments). A Couette cell geometry was placed on the Peltier device and filled with approximately 18 mL of the aqueous phase. Then, a diamond-shaped double-wall ring (DWR) made of Pt–Ir was placed at the air–water interface by monitoring the axial force drop. The DWR was then lowered by 500 μm to pin the interface.[47] After that, 5 mL of oil was added carefully against the wall of the Couette cell to avoid disturbing the interface and forming air bubbles. Plexiglass was used to cover the setup to minimize airflow during the experiment. The interface was allowed to equilibrate for 15 min. To determine the linear viscoelastic region, a dynamic strain sweep at 1 Hz was conducted from 0.01 to 100% strain, followed by a frequency sweep to measure the interfacial elastic, G', and viscous, G'', moduli as a function of the frequency.

Operando ultrasmall-/small-angle X-ray (USAXS/SAXS) experiments were performed at the advanced photon source (APS), Argonne National Laboratory. As reported elsewhere,[16,17] 50 μL of the nanoparticle suspension was added to a glass vial with a diameter of 5 mm, followed by injecting 50 μL of the oil. The X-ray flux is 10^{13} photon/mm^{2}s and the energy of the incident X-ray beam is 21.0 keV corresponding to a wavelength of 0.589 Å. Bonse–Hart and Pilatus 100 K pinhole cameras (Dectris Ltd., Baden, Switzerland) were used to collect the scattered USAXS and SAXS data, respectively. Nika and Irena software were used to reduce the 2D data to 1D.[48,49] Background scattering from the oil–brine or oil–DI water was collected and subtracted from the scattering profiles in the presence of the nanoparticles. Silver behenate was used to calibrate the sample-to-detector distance and geometry. When the interfacial region was detected, USAXS and SAXS measurements were collected for 60 min to characterize the dynamics of the assembly. The wavevector, denoted by Q, is calculated using the following equation

$$Q = \frac{4\pi}{\lambda}\sin\theta \tag{3}$$

where λ is the radiation wavelength and θ is the scattering angle.

AFM experiments were performed using PeakForce Tapping mode on a Multimode 8 (Nanoscope 6) in air and in liquid using a silicon tip on a nitride cantilever (SCAN ASYST-AIR probe with spring constant of 0.4 N/m for dry measurements and Peakforce-HIRS-F-A probe with spring constant of 0.35 N/m for liquid measurements). The Si wafers (p-type Si, single side polished, purchased from Pure Wafer) were cleaned before use for 15 min in an ultrasonic bath (160 W) with water, acetone, and ethanol. For imaging in air, NPs were deposited from 0.05 wt % aqueous dispersions onto silicon wafers by drop casting. For the liquid AFM measurements, a 100 μL droplet of the aqueous dispersions of the NPs was placed on the silicon wafer and allowed to dry. A droplet of DI water was placed on the sample and on the tip and allowed to equilibrate for 20 min prior to the measurements in the fluid cell. In some experiments, an oil droplet was placed on top to completely cover the aqueous phase.

RESULTS AND DISCUSSION

Materials Characterization. The SiO_2 NPs functionalized with the mixture of silanes (referred to as $S_{1,2}$) show a spherical morphology with an average diameter of 15 ± 3 nm (based on the measurement from TEM and AFM) (Figure 1c,f). The grafted silane layer increases the average diameter of $S_{1,2}$ by 3 nm compared to the core silica (the size of HS-30 colloidal silica NPs was 12 ± 3 nm). The organic content for $S_{1,2}$ as determined by TGA is 10 wt %. Using a 1:1 ratio of grafted silanes (see XPS analysis below), the organic content corresponds to a surface coverage of 43% (based on 5 OH/nm^2).[50] Grafting of the silanes on the NPs was further confirmed by XPS. The wide scan survey shows peaks at about 400 and 285 eV corresponding to N 1s and C 1s, respectively. Deconvolution of the high-resolution spectrum of the N 1s core region reveals three types of nitrogen species present at 398, 401, and 402.5 eV, which correspond to the primary and secondary amine and quaternary ammonium groups, respectively. Quantification of the XPS spectra shows that the ratio of the two silanes on $S_{1,2}$ is 1:1.[41] Consistent with the XPS analysis (the presence of quaternary ammonium groups and primary and secondary amine groups that are protonated at pH 7), the particles show an average ζ-potential of $+30 \pm 2$ mV. In contrast, the silica NPs before surface functionalization are negatively charged with a ζ-potential of -25 mV at neutral pH.[41]

For the S_1 silica (NPs functionalized with *N*-trimethoxysilylpropyl-*N,N,N*-trimethylammonium, TMA), the organic content is 4.2%, which corresponds to a surface coverage of 22%. The size of S_1 particles determined by TEM and AFM as described above is 15 ± 2 nm (Figure 1a,d). The corresponding values for S_2 (functionalized with N1-(3-trimethoxysilylpropyl) diethylenetriamine (TMPA)) are size 15 ± 4 nm (Figure 1b,e), organic content 6.7 wt %, and surface coverage 24%. Both S_1 and S_2 are positively charged in DI water with a ζ-potential in DI water similar to $S_{1,2}$ ($+30$ mV).

Atomic force microscopy was used to quantify changes in the surface roughness due to silane grafting on the silica surface. Under dry conditions, the average surface roughness increased from 0.2 nm in the starting colloidal silica to 0.87 ± 0.3, 1.2 ± 0.1, and 1.4 ± 0.2 nm for S_1, S_2, and $S_{1,2}$, respectively. When the NPs are placed in DI water, their roughness increases somewhat compared to that under dry conditions. The small increase is most likely due to hydration of the polar surface groups. The roughness for S_1, S_2, and $S_{1,2}$ in DI water is 0.9 ± 0.3, 1.5 ± 0.3, and 1.7 ± 0.4 nm. That is the roughness increases in the order $S_1 < S_2 < S_{1,2}$, regardless of

whether the particles are dry or in DI water. These data are summarized in Table 1.

Table 1. Summary of Surface Properties of the Different NP Systems

NPs system	organic content (wt %)	grafting efficiency (%)	roughness dry (nm)	roughness in DI (nm)	ζ-potential (mV)
S_1	4.2	22	0.87 ± 0.3	0.9 ± 0.3	30 ± 2
S_2	6.7	24	1.2 ± 0.1	1.5 ± 0.3	31 ± 3
$S_{1,2}$	10	43	1.4 ± 0.2	1.7 ± 0.4	30 ± 2

Colloidal Stability of the Suspension. One of the challenges of using NPs in practical applications is their colloidal stability, especially in high salinity and high charge electrolytes. With increasing ion concentration, the surface charge on the particles is screened resulting in aggregation and sedimentation.[19,51,52] In the following section, we focus on the stability of NPs in a complex brine containing a mixture of salts (701, 22, 185, 44, and 1.6 mM NaCl, $CaCl_2$, $MgCl_2$ Na_2SO_4, and $NaHCO_3$, respectively) and different temperatures (up to 60 °C) under accelerated test conditions. We start with suspensions of $S_{1,2}$ (1 wt %) subjected to $500 \times \vec{g}$ at different temperatures for 500 s. We quantify the stability by the separation indices at different temperatures, calculated from the transmission profiles (Figure 2a). Recall that the separation
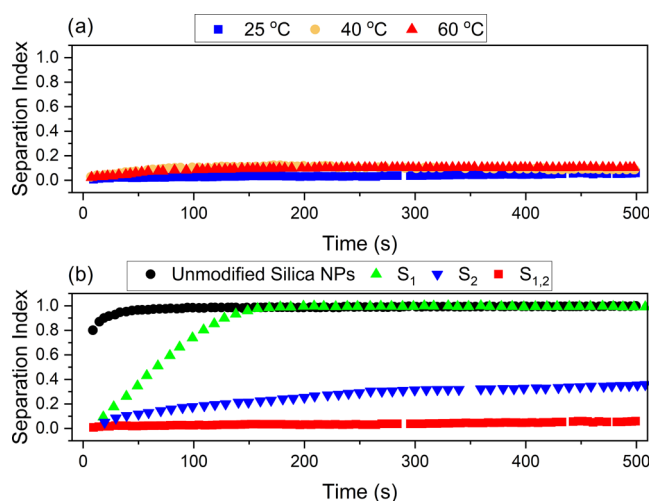

Figure 2. (a) Separation indices for 1 wt % suspension in brine of $S_{1,2}$ NPs modified with the mixture of two silanes at 25 °C (blue), 40 °C (orange), and 60 °C (red). (b) Separation indices for the different NP systems in brine (black: unmodified NPs, green: S_1, blue: S_2 and red: $S_{1,2}$) indicating the stability of the double-functionalized system in comparison to the single-functionalized particles and the unmodified silica NPs.

index for a stable suspension is 0. On the other hand, a separation index of 1 corresponds to complete particle separation and sedimentation. The separation index for $S_{1,2}$ at 25 °C is basically zero. At 60 °C, the separation index gradually increases to 0.1 (10%) in the first 70 s and then remains unchanged. For comparison, when the unmodified silica NPs were suspended in brine, the particles aggregated immediately even at room temperature (Figure 2b). The transmission of the suspension increased quickly, and the separation index reached 1 in about 50 s. It is also worth
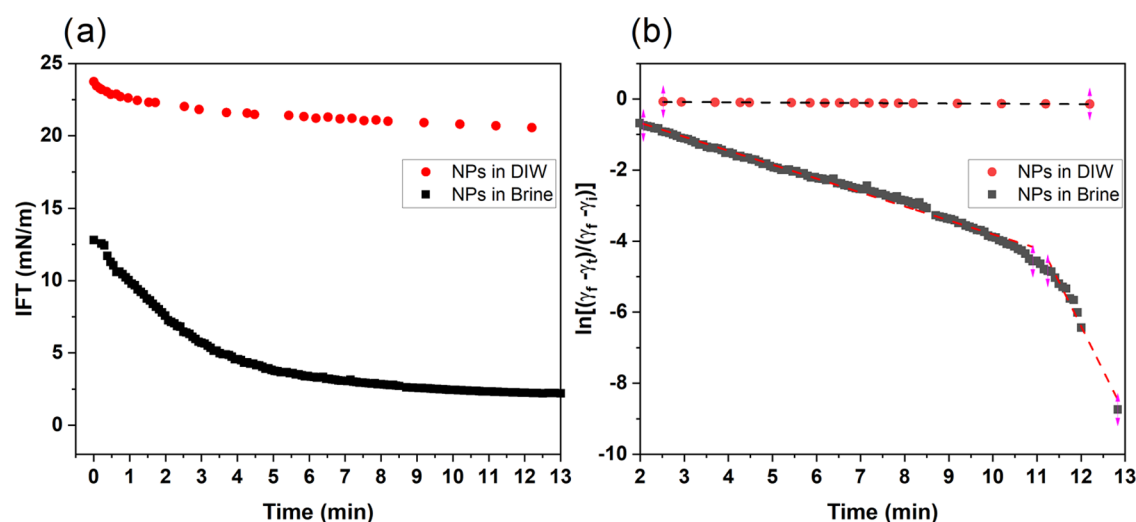
Figure 3. (a) Dynamic interfacial tension of oil−water when 1 wt % NP suspension in brine (black) and DI water (red) was used. (b) Natural log fit of the dynamic data with the dashed lines representing a linear fit of the selected portions.

mentioning that, when the $S_{1,2}$ suspension was stored in brine for 3 months, the separation profile was similar to the fresh sample, suggesting an excellent shelf life of the suspension.

We further compare the colloidal stability of $S_{1,2}$ to suspensions of particles functionalized with either one of the silanes (S_1 and S_2). As shown in Figure 2b, S_1 is the least stable, with complete separation after 150 s. On the other hand, S_2 shows a separation index of about 0.2 in 100 s and continues to increase reaching a plateau of 0.35 in 300 s.

The stability of the particles grafted with different silanes was correlated to salt adsorption using QCM (Figure S1a) and ζ-potential measurements (Figure S1b). For the QCM measurements, after deposition of the particles onto the quartz crystal and placement of the sensor in DI water to establish a stable baseline, a solution of the brine is injected for 30 min, followed by rinsing with DI water. The amount of brine adsorbed by the $S_{1,2}$ particles calculated from the change in frequency using eq 2 is 23 times lower compared to S_1. In addition, the adsorption is reversible, as the frequency difference after the DI water rinse approaches zero. This is contrasted with the slower return to the baseline for S_2. The behavior of the different NP systems to electrolyte adsorption is in excellent agreement with both the ζ-potential and the accelerated stability tests.

Figure S1b shows the zeta-potential for the different NPs at various concentrations of brine. All NP systems (S_1, S_2, and $S_{1,2}$) show the same ζ-potential in DI water (approximately +30 mV). However, when suspended in a diluted brine (5700 ppm), the single-functionalized particles show a steep decrease in ζ-potential. The ζ-potentials become +13 and +18 mV for the S_1 and S_2 particles, respectively. In contrast, the ζ-potential of the double-functionalized particles ($S_{1,2}$) in the same brine concentration is +25 mV. Increasing the salt concentration results in similar trends, although the high salt concentration (higher conductivity of the medium) introduces a larger error and makes the ζ-potential measurements less reliable. Nevertheless, the effective charge screening of the S_1 and S_2 particles significantly affects their colloidal stability significantly. In contrast, the charge of $S_{1,2}$ does not seem to be screened as effectively resulting in higher stability even in a high ionic strength brine.

Recall that S_1 is functionalized with a silane terminated in a permanently charged ammonium group, while S_2 is functionalized with a silane bearing both primary and secondary amine groups that are protonated at neutral pH. On the other hand, $S_{1,2}$ contains a 1:1 ratio of both silanes. Furthermore, the coverage with the silane molecules increases in the order $S_1 < S_2 < S_{1,2}$. The increased coverage of $S_{1,2}$ and the presence of both silanes resulting in a random, disordered structure, forces the silane molecules to adopt a more extended configuration (recall the grafted layer of $S_{1,2}$ and the surface roughness is the highest). We believe this extended arrangement of the silanes and rougher surface structure results in different water structures around the particles, which, in turn, influences the ability of ions to interact. The reduced number of ions adsorbed and the reversible nature of the interaction signify a reduced interaction, which results in less effective charge screening and, thus, higher colloidal stability. In addition, it has been reported that increasing the chemical heterogeneity and/or surface roughness (i.e., by using two different silanes on the surface of the particle) contributes to higher colloidal stability under high salinity conditions. Specifically, the surface roughness becomes a contributing factor to the stability of colloids, when the Debye length becomes smaller than the surface roughness.[53,54]

Interfacial Assembly. Next, we turn our attention to the NP assembly at the oil−water interface. In this section, we study both the interfacial structure as well as the dynamics of the process and relate to the resulting interfacial properties. Since $S_{1,2}$ shows better colloidal stability than either S_1 or S_2; henceforth, we focus on $S_{1,2}$. We use crude oil and, in some cases, model oil as substrates for interfacial studies. Both of these systems bear permanent negative surface charges in water at neutral pH (ζ-potential = -52 ± 3 mV and -34 ± 5, respectively) due to the presence of deprotonated carboxylic acid groups.[24,41,55] These permanent charges differ from the charges developed at a neat hydrocarbon−water interface, which are due to the adsorption of hydroxyl groups on the hydrocarbon surface from water.[41,56]

The interfacial tension, IFT, as a function of time for crude oil in a 1 wt % suspension of $S_{1,2}$ in DI water is shown in Figure 3a. First, there is a fast drop in IFT to about 25 mN/m (the IFT is 32 mN/m when no NPs are present) followed by a slow

decrease. The IFT reaches 20 mN/m after 13 min. In contrast, when a 1 wt % suspension of the $S_{1,2}$ particles in brine is used, the IFT decreases fast initially followed by a slower decrease and it reaches a plateau value of 2.1 mN/m (equilibrium IFT) after ~10 min.

The particle assembly can be divided into three steps: (1) diffusion of the particles to the interface, (2) reaction of the positively charged particles with the negatively charged oil surface, and (3) reorganization of the particles at the interface to complete particle coverage. For a diffusion-controlled process, a plot of IFT vs $t^{1/2}$ should be linear.[57] Indeed, the early stages of the IFT vs $t^{1/2}$ (i.e., 0−200 s) are linear with slopes of 0.15 and 0.64 mN/m.s$^{1/2}$ for particle suspensions in DI water and brine, respectively. The particle diffusion rate constant is somewhat faster in brine than in DI water consistent with faster diffusion when ions are present and the particle surface charges are screened.[26,57,58]

The IFT as a function of time, t, can also be fitted to a first-order model[47,59]

$$\ln\left[\frac{\gamma_f - \gamma_t}{\gamma_f - \gamma_i}\right] = -k_i t \tag{4}$$

where γ_f, γ_t, γ_i, and k_i are the final IFT, the IFT at time t, the initial IFT, and the rate constant, respectively. Figure 3b shows the fit using the above equation. For suspensions in DI water, the dynamic IFT is described by a single process with a rate constant of 1.1×10^{-4} s^{-1}. In contrast, the IFT for suspensions in brine shows two distinct regimes with rate constants of 6.4×10^{-3} and 4.5×10^{-2} s^{-1}, respectively. We attribute the first rate constant to the particles reacting/decorating the interface, while the second to subsequent particle reorganization to complete the particle coverage at the interface. The rate constant in brine is 60 times higher compared to DI water consistent with the particle adsorption being faster in the presence of electrolytes.[58] We find that for suspensions in DI water, there is no subsequent step to complete the particle coverage at the interface probably due to the higher interparticle repulsion in DI water that prevents the particles from forming a dense monolayer.[58] We also find that the reorganization step to complete the coverage is 7 times faster than that of particles reacting with the oil surface.

The adsorption energy and surface coverage of the different systems can be estimated from dynamic interfacial tension experiments. For the suspension in brine, the surface coverage reaches the theoretical value of a hexagonal close-packed assembly (0.91) in 13 min. The corresponding value for the NPs in DI water after the same amount of time was 0.6. Moreover, the adsorption energy is approximately 2400 and 1000 $K_b T$ for the particles in brine and DI water, respectively. The calculated values are in agreement with the expected adsorption energy of a particle with a diameter of 15 nm and a three-phase contact angle of 70°, where the attachment energy is in the order of 10^3 $K_b T$.[60]

The analysis of the IFT is corroborated with USAXSS/SAXS measurements. Figure 4a,b shows the scattering profiles of the oil−water interface for 1 wt % suspensions of NPs in brine or DI water. The scattering profiles are consistent with the assembly of spherical NPs at the interface.[16] While both systems show that NPs are present at the interface, the difference in behavior becomes apparent when we compare the time dependence of assembly. As shown in Figure 4a, the scattering intensity in the USAXS region (low Q region) for
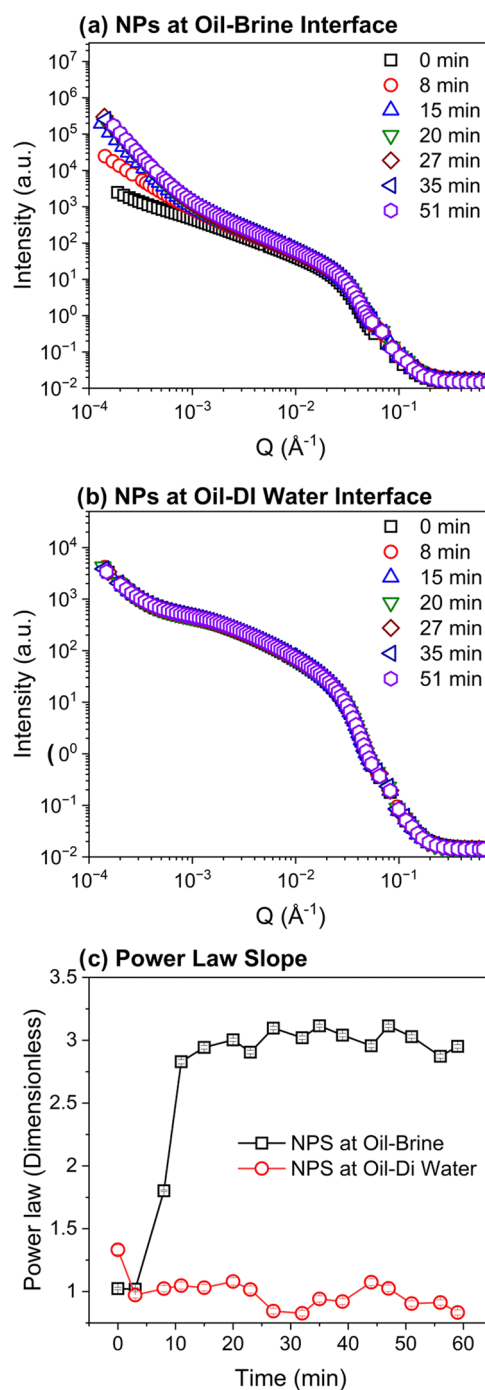

Figure 4. USAXS/SAXS measurements for the assembly of silica particles at the oil−water interface: (a) NPs in brine, (b) NPs in DI water, and (c) evolution of the power law slope for NPs in DI water (red circles) and NPs in brine (black squares).

the particles in brine increases with time and stabilizes after about 10 min. In contrast, for the particles in DI water, the assembly shows no time dependence (Figure 4b). These results are consistent with the IFT behavior described earlier. Recall that the IFT of the particles in DI water is virtually unchanged with time but keeps decreasing with time for suspensions in brine. The morphology of the assembled particles is further characterized by calculating the power law slope in the USAXS region ($Q < 5 \times 10^{-4}$ Å^{-1}). Figure 4c shows that the power law slope for NPs in brine increases
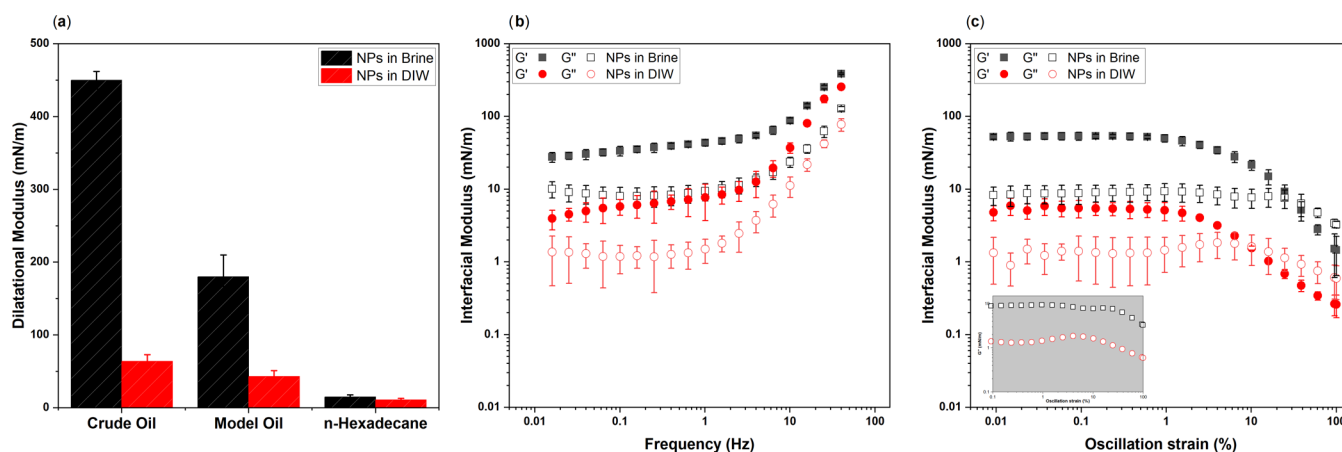
Figure 5. (a) Comparison of the interfacial dilatational modulus for 1 wt % particle suspension in brine (black bars) and in DI water (red bars) for crude oil and model oil. (b) Interfacial storage (filled symbols) and loss modulus (open symbols) as a function of frequency for crude oil−water when 1 wt % NP suspension in brine (black) and DI water (red) are used. (c) Similar but as a function of strain at 1 Hz. The inset in panel (c) is an expanded plot that shows the presence of one (NPs in DI water) and two (NPs in brine) relaxation peaks.

quickly, reaching a value of 3 after about 10 min. This behavior agrees well with the IFT experiments (Figure 3a), where the IFT reaches an equilibrium value in ∼10 min. For comparison, the power slope of the particles in DI water remains constant with time with a value of ∼1, indicative of an interface where particles form a very open structure (what we might refer to as a mass fractal in 3D).[17] For the particles in brine, the slope starts at 1 similar to that in DI water, but it increases quickly before it plateaus to a value of 3 after about 10 min. The latter slope is consistent with particles in a dense assembly (the analogue in 3D of a smooth, dense structure).

In the next section, we focus on the mechanical properties of the interface in the presence of NPs. We start with measurements of the dilatational modulus, followed by experiments in shear. As shown in Figure 5a, the dilatational modulus of the crude oil−water interface for 1 wt % suspensions in DI water is 65 mN/m. The dilatational modulus for the same particle suspension in brine reached 450 mN/m. This large increase in modulus can be reached even at a much lower concentration of particles in brine (0.25 wt %). In contrast, the interfacial modulus for a pure hydrocarbon (hexadecane) in 1 wt % suspension of particles either in water or brine is much lower (11 ± 2 and 15 ± 3 mN/m) underlying the importance of having complementary permanent charges at the interface. Recall that hexadecane has a ζ-potential of approximately −30 mV in DI water due to the adsorption of OH groups on the surface but not permanent charges.[60] The presence of permanent charges is further confirmed by adding 10 mM stearic acid to hexadecane (model oil), where the dilatational modulus increases from 15 ± 3 to about 180 ± 30 mN/m when a suspension of nanoparticles is used in brine and from 11 ± 2 to 28 ± 2 mN/m when the suspension is in DI water.

The interfacial behavior above is consistent with the experiments in shear. When the NPs are in brine, the storage modulus is nearly independent of frequency, suggesting a solid-like interface (Figure 5b). In addition, the interfacial storage modulus in brine is ∼7-fold higher compared to that in DI water. Moreover, the interfacial tan (δ), which is the ratio of the loss modulus to the storage modulus, is the lowest for the suspension of NPs in brine, consistent with its solid-like character. The interfacial tan (δ) is nearly 1 when NPs are not present (i.e., oil−DI water).[61,62] Finally, when NPs are present at the interface, the crossover strain, where the storage and loss moduli become equal in the strain sweep signifying the transition from solid-like to liquid-like, is 10% in DI water but 50% in brine consistent with a less deformable interface for the latter (Figure 5c).[63]

Looking closer, we see (Figure 5c) that the interfacial G'' for the NPs in DI water exhibits a single peak at 4% strain. In contrast, the G'' in brine shows two such peaks: one at about 1% and another at 16% strain. Based on ideas developed for colloidal glasses[64,65] and consistent with the dynamics of the assembly as we discussed above, where the assembly in DI water is characterized by one step but by two steps in brine, we attribute the single peak of interfacial G'' for the system in DI water to the bond breaking between the particles and the oil surface. In other words, the interface would dynamically be distorted to a strain of 4% without altering the underlying structure, but once that strain value is reached, it starts deforming as the oil−particle bonds start breaking. On the other hand, a strain of 1% is enough to start breaking first the interparticle interactions creating a loosened particle layer, but it takes a strain of 16% to break the bonds between the particles and the oil, remove the particle assembly at the interface, and return to a liquid-like behavior. As expected, for a liquid-like behavior at that point, the loss modulus is higher than the storage modulus.[66]

The less deformable interface can be seen macroscopically by observing the shape of oil droplets after spinning at 10 000 rpm and subsequently bringing back to rest (0 rpm) (Figure S2). For the systems in the absence of NPs, the oil droplet returned to its equilibrium spherical shape when it returned to 0 rpm. In contrast, when the NPs were present in the brine, the oil droplets remained deformed in a nonequilibrium ellipsoidal shape because of the higher modulus; that is, the interface is jammed and becomes less deformable.

To sum it up, although particle assembly does take place from suspensions in either DI water or brine, the interface becomes solid-like and behaves like an elastic membrane as we demonstrate below only in the case of the particle suspension in brine. Videos 1,2 and Figure S3 in the SI show the reaction to an AFM tip pushed against the oil−water interface. As can be seen in the videos, the AFM tip can easily pierce through

the interface when the NPs are suspended in DI water. In contrast, when the NPs are suspended in brine, the AFM tip encounters resistance similar to that of an elastic membrane (solid but deformable), as evident from the presence of the wrinkles formed during deformation of the interface. This elastic, deformable oil−water interface translates into significant changes in the stability of the emulsion. As shown in Videos 3,4 in the SI, when two oil droplets are pushed against each other, they coalesce when the NPs are suspended in DI water but resist coalescence, when the NPs are suspended in brine. A clear deformation of the droplets can be seen for the latter, but no coalescence occurs.

CONCLUSIONS

The colloidal stability of silica NPs functionalized simultaneously with two different silanes and their assembly at oil−water interfaces was studied under various environments. Using accelerated tests, we demonstrate that the particles were stable in high salinity brine and high temperature for extended periods of time, even when subjected to accelerated separation conditions. In contrast, the colloidal stability of the particles functionalized with either silane under identical conditions was much lower. The difference in colloidal stability was related to the amount and roughness of the grafted silane layers, which influence the ability of ions to interact with the NPs and screen their surface charge. Using the colloidally stable silica NPs, we studied the assembly mechanism at oil−water interfaces using static- and time-dependent measurements, including in operando ultrasmall-/small-angle X-ray scattering (USAXS/SAXS). We find that the process in DI water is characterized by a single step, while that in brine is made up of an additional step that leads to a denser, smoother NP layer assembled at the interface. This second step in the assembly is critical to the interface becoming solid-like, as illustrated by measurements of the interfacial dilatational and shear moduli as well as looking at its macroscopic behavior.

ASSOCIATED CONTENT

Ⓢ Supporting Information

The Supporting Information is available free of charge at https://pubs.acs.org/doi/10.1021/acs.chemmater.3c01871.

> QCM and ζ-potential data for the different NP systems in brine; response of oil droplets to 10 000 rpm and at rest; response of the interfacial layer to the AFM tip; and videos demonstrating the response of the interface to the AFM tip piercing through the interface, and coalescence and stability of oil droplets (PDF)

AUTHOR INFORMATION

Corresponding Author

Emmanuel P. Giannelis − *Department of Materials Science and Engineering, Cornell University, Ithaca, New York 14850, United States*; Email: epg2@cornell.edu

Authors

Ahmed Wasel Alsmaeil − *Department of the Chemical and Biomolecular Engineering, Cornell University, Ithaca, New York 14850, United States; EXPEC Advanced Research Center, Saudi Aramco, Dhahran 31261, Saudi Arabia;* ⓞ orcid.org/0000-0001-7121-9876

Sohaib Mohammed − *School of Civil and Environmental Engineering, Cornell University, Ithaca, New York 14850, United States;* ⓞ orcid.org/0000-0002-0262-9481

Bashayer Saad Aldakkan − *EXPEC Advanced Research Center, Saudi Aramco, Dhahran 31261, Saudi Arabia; Department of Materials Science and Engineering, Cornell University, Ithaca, New York 14850, United States;* ⓞ orcid.org/0000-0001-9025-540X

Nikolaos Chalmpes − *Department of Materials Science and Engineering, Cornell University, Ithaca, New York 14850, United States;* ⓞ orcid.org/0000-0003-2744-5934

Antonios Kouloumpis − *Department of Materials Science and Engineering, Cornell University, Ithaca, New York 14850, United States;* ⓞ orcid.org/0000-0002-8738-3141

Georgia Potsi − *Department of Materials Science and Engineering, Cornell University, Ithaca, New York 14850, United States*

Andrew Galvin − *Department of Materials Science and Engineering, Cornell University, Ithaca, New York 14850, United States*

Greeshma Gadikota − *Department of the Chemical and Biomolecular Engineering, Cornell University, Ithaca, New York 14850, United States; School of Civil and Environmental Engineering, Cornell University, Ithaca, New York 14850, United States;* ⓞ orcid.org/0000-0002-6527-8316

Mazen Yousef Kanj − *College of Petroleum Engineering and Geosciences, King Fahd University of Petroleum & Minerals, Dhahran 31261, Saudi Arabia;* ⓞ orcid.org/0000-0002-2674-4505

Complete contact information is available at:
https://pubs.acs.org/10.1021/acs.chemmater.3c01871

Author Contributions

A.W.A. conducted the experiments and wrote the manuscript. S.M. performed the USAXS/SAXS experiments. A.K. helped in the synthesis and performed the AFM experiments. G.P. helped in the synthesis and performed the XPS experiment. N.C. and B.S.A. performed the surface characterization with the AFM. A.G. conducted the IFT experiments. G.G. suggested experiments and guided the USAXS/SAXS analysis. M.Y.K. offered guidance in the research. E.P.G. guided the work and recommended experiments. All authors discussed and commented on the manuscript.

Notes

The authors declare no competing financial interest.

■ REFERENCES

(1) Kang, H.; Long, D. J.; Haynes, C. L. Preparation of Colloidally Stable Positively Charged Hollow Silica Nanoparticles: Effect of Minimizing Hydrolysis on ζ Potentials. *Langmuir* **2019**, *35* (24), 7985−7994.

(2) Lecot, S.; Lavigne, A.; Yang, Z.; Géhin, T.; Botella, C.; Jousseaume, V.; Chevolot, Y.; Phaner-Goutorbe, M.; Yeromonahos, C. Arrangement of Monofunctional Silane Molecules on Silica Surfaces: Influence of Alkyl Chain Length, Head-Group Charge, and Surface Coverage, from Molecular Dynamics Simulations, X-Ray Photoelectron Spectroscopy, and Fourier Transform Infrared Spectroscopy. *J. Phys. Chem. C* **2020**, *124* (37), 20125−20134.

(3) Wang, L.; Schubert, U. S.; Hoeppener, S. Surface Chemical Reactions on Self-Assembled Silane Based Monolayers. *Chem. Soc. Rev.* **2021**, *50* (11), 6507−6540.

(4) Fernandes, N. J.; Wallin, T. J.; Vaia, R. A.; Koerner, H.; Giannelis, E. P. Nanoscale Ionic Materials. *Chem. Mater.* **2014**, *26* (1), 84−96.

(5) Shimada, T.; Aoki, K.; Shinoda, Y.; Nakamura, T.; Tokunaga, N.; Inagaki, S.; Hayashi, T. Functionalization on Silica Gel with Allylsilanes. A New Method of Covalent Attachment of Organic Functional Groups on Silica Gel. *J. Am. Chem. Soc.* **2003**, *125* (16), 4688−4689.

(6) Kang, T.; Jang, I.; Oh, S.-G. Surface Modification of Silica Nanoparticles Using Phenyl Trimethoxy Silane and Their Dispersion Stability in N-Methyl-2-Pyrrolidone. *Colloids Surf., A* **2016**, *501*, 24−31.

(7) Rostamzadeh, P.; Mirabedini, S. M.; Esfandeh, M. APS-Silane Modification of Silica Nanoparticles: Effect of Treatment's Variables on the Grafting Content and Colloidal Stability of the Nanoparticles. *J. Coat. Technol. Res.* **2014**, *11* (4), 651−660.

(8) Bouchoucha, M.; Côté, M.-F.; C -Gaudreault, R.; Fortin, M.-A.; Kleitz, F. Size-Controlled Functionalized Mesoporous Silica Nanoparticles for Tunable Drug Release and Enhanced Anti-Tumoral Activity. *Chem. Mater.* **2016**, *28* (12), 4243−4258.

(9) Mahtabani, A.; Rytöluoto, I.; Anyszka, R.; He, X.; Saarimäki, E.; Lahti, K.; Paajanen, M.; Dierkes, W.; Blume, A. On the Silica Surface Modification and Its Effect on Charge Trapping and Transport in PP-Based Dielectric Nanocomposites. *ACS Appl. Polym. Mater.* **2020**, *2* (8), 3148−3160.

(10) Graf, C.; Gao, Q.; Schütz, I.; Noufele, C. N.; Ruan, W.; Posselt, U.; Korotianskiy, E.; Nordmeyer, D.; Rancan, F.; Hadam, S.; Vogt, A.; Lademann, J.; Haucke, V.; Rühl, E. Surface Functionalization of Silica Nanoparticles Supports Colloidal Stability in Physiological Media and Facilitates Internalization in Cells. *Langmuir* **2012**, *28* (20), 7598−7613.

(11) Knowles, B. R.; Wagner, P.; Maclaughlin, S.; Higgins, M. J.; Molino, P. J. Modified Silica Nanoparticle Coatings: Dual Antifouling Effects of Self-Assembled Quaternary Ammonium and Zwitterionic Silanes. *Biointerphases* **2020**, *15* (2), No. 021009.

(12) Karnati, S. R.; Oldham, D.; Fini, E. H.; Zhang, L. Application of Surface-Modified Silica Nanoparticles with Dual Silane Coupling Agents in Bitumen for Performance Enhancement. *Constr. Build. Mater.* **2020**, *244*, No. 118324. DOI: 10.1016/j.conbuild-mat.2020.118324.

(13) Yang, X.-C.; Samanta, B.; Agasti, S. S.; Jeong, Y.; Zhu, Z.-J.; Rana, S.; Miranda, O. R.; Rotello, V. M. Drug Delivery Using Nanoparticle-Stabilized Nanocapsules. *Angew. Chem., Int. Ed.* **2011**, *50* (2), 477−481.

(14) Hammami, M. A.; Kanj, M. Y.; Giannelis, E. P. Monitoring the Early Stages of Formation of Oil-Water Emulsions Using Flow Cytometry. *Langmuir* **2022**, *38* (1), 62−71.

(15) Alsmaeil, A. W.; Hammami, M. A.; Enotiadis, A.; Kanj, M. Y.; Giannelis, E. P. Encapsulation of an Anionic Surfactant into Hollow Spherical Nanosized Capsules: Size Control, Slow Release, and Potential Use for Enhanced Oil Recovery Applications and Environmental Remediation. *ACS Omega* **2021**, *6* (8), 5689−5697.

(16) Mohammed, S.; Kuzmenko, I.; Gadikota, G. Reversible Assembly of Silica Nanoparticles at Water−Hydrocarbon Interfaces Controlled by SDS Surfactant. *Nanoscale* **2021**, *14* (1), 127−139.

(17) Mohammed, S.; Asgar, H.; Kuzmenko, I.; Gadikota, G. Self-Assembly of Silica Nanoparticles at Water−Hydrocarbon Interfaces: Insights from In Operando Small-Angle X-Ray Scattering Measurements and Molecular Dynamics Simulations. *Energy Fuels* **2020**, *34* (10), 12545−12555.

(18) Guzmán, E.; Martínez-Pedrero, F.; Calero, C.; Maestro, A.; Ortega, F.; Rubio, R. G. A Broad Perspective to Particle-Laden Fluid Interfaces Systems: From Chemically Homogeneous Particles to Active Colloids. *Adv. Colloid Interface Sci.* **2022**, *302*, No. 102620.

(19) Vasantha, V. A.; Hua, N. Q.; Rusli, W.; Hadia, N. J.; Stubbs, L. P. Unique Oil-in-Brine Pickering Emulsion Using Responsive Antipolyelectrolyte Functionalized Latex: A Versatile Emulsion Stabilizer. *ACS Appl. Mater. Interfaces* **2020**, *12* (20), 23443−23452.

(20) Lee, J. G.; Larive, L. L.; Valsaraj, K. T.; Bharti, B. Binding of Lignin Nanoparticles at Oil−Water Interfaces: An Ecofriendly Alternative to Oil Spill Recovery. *ACS Appl. Mater. Interfaces* **2018**, *10* (49), 43282−43289.

(21) Goldhahn, C.; Schubert, J.; Schlaad, H.; Ferri, J. K.; Fery, A.; Chanana, M. Synthesis of Metal@Protein@Polymer Nanoparticles with Distinct Interfacial and Phase Transfer Behavior. *Chem. Mater.* **2018**, *30* (19), 6717−6727.

(22) Zhang, F.; Yang, F.; Hua, M.; Yang, Z.; Wei, H.; Yang, Y.; Wei, J. Buckling of Two-Dimensional Colloidal Nanoplatelets in Confined Space To Design Heterogeneous Catalysts. *Chem. Mater.* **2019**, *31* (10), 3812−3817.

(23) Aldakkan, B. S.; Hammami, M. A.; Qi, G.; Kanj, M. Y.; Giannelis, E. P. Stimuli-Responsive, Hydrolyzable Poly(Vinyl Laurate-Co-Vinyl Acetate) Nanoparticle Platform for In Situ Release of Surfactants. *ACS Appl. Mater. Interfaces* **2021**, *13* (21), 25553−25562.

(24) Hammami, M. A.; Kouloumpis, A.; Qi, G.; Alsmaeil, A. W.; Aldakkan, B.; Kanj, M. Y.; Giannelis, E. P. Probing the Mechanism of Targeted Delivery of Molecular Surfactants Loaded into Nanoparticles after Their Assembly at Oil−Water Interfaces. *ACS Appl. Mater. Interfaces* **2023**, *15* (4), 6113−6122.

(25) Kanj, M.; Sakthivel, S.; Giannelis, E. Wettability Alteration in Carbonate Reservoirs by Carbon Nanofluids. *Colloids Surf., A* **2020**, *598*, No. 124819.

(26) Shi, S.; Russell, T. P. Nanoparticle Assembly at Liquid−Liquid Interfaces: From the Nanoscale to Mesoscale. *Adv. Mater.* **2018**, *30* (44), No. 1800714.

(27) Xu, R.; Liu, T.; Sun, H.; Wang, B.; Shi, S.; Russell, T. P. Interfacial Assembly and Jamming of Polyelectrolyte Surfactants: A Simple Route To Print Liquids in Low-Viscosity Solution. *ACS Appl. Mater. Interfaces* **2020**, *12* (15), 18116−18122.

(28) Sun, J.; Yi, C.; Wei, W.; Zhao, D.; Hu, Q.; Liu, X. Nanohybrids from Direct Chemical Self-Assembly of Poly(Styrene-Alt-Maleic Anhydride) as PH-Responsive Particulate Emulsifiers. *Langmuir* **2014**, *30* (49), 14757−14764.

(29) Xue, W.; Yang, H.; Du, Z. Synthesis of PH-Responsive Inorganic Janus Nanoparticles and Experimental Investigation of the Stability of Their Pickering Emulsions. *Langmuir* **2017**, *33* (39), 10283−10290.

(30) Cui, M.; Emrick, T.; Russell, T. P. Stabilizing Liquid Drops in Nonequilibrium Shapes by the Interfacial Jamming of Nanoparticles. *Science* **2013**, *342* (6157), 460−463.

(31) Ali, N.; Bilal, M.; Khan, A.; Ali, F.; Yang, Y.; Khan, M.; Adil, S. F.; Iqbal, H. M. N. Dynamics of Oil-Water Interface Demulsification Using Multifunctional Magnetic Hybrid and Assembly Materials. *J. Mol. Liq.* **2020**, *312*, No. 113434.

(32) Ali, N.; Zhang, B.; Zhang, H.; Zaman, W.; Li, X.; Li, W.; Zhang, Q. Interfacially Active and Magnetically Responsive Composite Nanoparticles with Raspberry like Structure; Synthesis and Its Applications for Heavy Crude Oil/Water Separation. *Colloids Surf., A* **2015**, *472*, 38−49.

(33) Tang, J.; Quinlan, P. J.; Tam, K. C. Stimuli-Responsive Pickering Emulsions: Recent Advances and Potential Applications. *Soft Matter* **2015**, *11* (18), 3512−3529.

(34) Gao, P.; Xing, X.; Li, Y.; Ngai, T.; Jin, F. Charging and Discharging of Single Colloidal Particles at Oil/Water Interfaces. *Sci. Rep.* **2014**, *4* (1), No. 4778.

(35) Bergfreund, J.; Sun, Q.; Fischer, P.; Bertsch, P. Adsorption of Charged Anisotropic Nanoparticles at Oil−Water Interfaces. *Nanoscale Adv.* **2019**, *1* (11), 4308−4312.

(36) Chai, Y.; Lukito, A.; Jiang, Y.; Ashby, P. D.; Russell, T. P. Fine-Tuning Nanoparticle Packing at Water−Oil Interfaces Using Ionic Strength. *Nano Lett.* **2017**, *17* (10), 6453−6457.

(37) Da, C.; Zhang, X.; Alzobaidi, S.; Hu, D.; Wu, P.; Johnston, K. P. Tuning Surface Chemistry and Ionic Strength to Control Nanoparticle Adsorption and Elastic Dilational Modulus at Air-Brine Interface. *Langmuir* **2021**, *37* (19), 5795−5809.

(38) Zhang, X.; Servos, M. R.; Liu, J. Ultrahigh Nanoparticle Stability against Salt, PH, and Solvent with Retained Surface Accessibility via Depletion Stabilization. *J. Am. Chem. Soc.* **2012**, *134* (24), 9910−9913.

(39) Metin, C. O.; Lake, L. W.; Miranda, C. R.; Nguyen, Q. P. Stability of Aqueous Silica Nanoparticle Dispersions. *J. Nanopart. Res.* **2011**, *13* (2), 839−850.

(40) Luo, D.; Wang, F.; Alam, M. K.; Yu, F.; Mishra, I. K.; Bao, J.; Willson, R. C.; Ren, Z. Colloidal Stability of Graphene-Based Amphiphilic Janus Nanosheet Fluid. *Chem. Mater.* **2017**, *29* (8), 3454−3460.

(41) Alsmaeil, A. W.; Kouloumpis, A.; Potsi, G.; Hammami, M. A.; Kanj, M. Y.; Giannelis, E. P. Probing the Interfacial Properties of Oil−Water Interfaces Decorated with Ionizable, PH Responsive Silica Nanoparticles. *Langmuir* **2023**, *39* (8), 3118−3130.

(42) Bapat, S.; Giehl, C.; Kohsakowski, S.; Peinecke, V.; Schäffler, M.; Segets, D. On the State and Stability of Fuel Cell Catalyst Inks. *Adv. Powder Technol.* **2021**, *32* (10), 3845−3859.

(43) Huang, J.; Zajforoushan Moghaddam, S.; Thormann, E. Structural Investigation of a Self-Cross-Linked Chitosan/Alginate Dialdehyde Multilayered Film with in Situ QCM-D and Spectroscopic Ellipsometry. *ACS Omega* **2019**, *4* (1), 2019−2029.

(44) Manga, M. S.; Hunter, T. N.; Cayre, O. J.; York, D. W.; Reichert, M. D.; Anna, S. L.; Walker, L. M.; Williams, R. A.; Biggs, S. R. Measurements of Submicron Particle Adsorption and Particle Film Elasticity at Oil−Water Interfaces. *Langmuir* **2016**, *32* (17), 4125−4133.

(45) Hsieh, T.-L.; Martinez, M. R.; Garoff, S.; Matyjaszewski, K.; Tilton, R. D. Interfacial Dilatational Rheology as a Bridge to Connect Amphiphilic Heterografted Bottlebrush Copolymer Architecture to Emulsifying Efficiency. *J. Colloid Interface Sci.* **2021**, *581*, 135−147.

(46) Marquez, R.; Acevedo, N.; Rondón, M.; Graciaa, A.; Daridon, J.-L.; Salager, J.-L. Breaking of Water-in-Crude Oil Emulsions. 10. Experimental Evidence from a Quartz Crystal Resonator Sensor and an Oscillating Spinning Drop Interfacial Rheometer. *Energy Fuels* **2023**, *37* (4), 2735−2749.

(47) Wu, M.; Zhang, H. Determination of the Emulsion Stabilization Mechanisms of Quaternized Glucan of Curdlan via Rheological and Interfacial Characterization. *Langmuir* **2023**, *39* (8), 3029−3044.

(48) Ilavsky, J. Nika: Software for Two-Dimensional Data Reduction. *J. Appl. Crystallogr.* **2012**, *45* (2), 324−328.

(49) Ilavsky, J.; Jemian, P. R. Irena: Tool Suite for Modeling and Analysis of Small-Angle Scattering. *J. Appl. Crystallogr.* **2009**, *42* (2), 347−353.

(50) Zhao, X. S.; Lu, G. Q.; Whittaker, A. K.; Millar, G. J.; Zhu, H. Y. Comprehensive Study of Surface Chemistry of MCM-41 Using 29Si CP/MAS NMR, FTIR, Pyridine-TPD, and TGA. *J. Phys. Chem. B* **1997**, *101* (33), 6525−6531.

(51) Bagaria, H. G.; Yoon, K. Y.; Neilson, B. M.; Cheng, V.; Lee, J. H.; Worthen, A. J.; Xue, Z.; Huh, C.; Bryant, S. L.; Bielawski, C. W.; Johnston, K. P. Stabilization of Iron Oxide Nanoparticles in High Sodium and Calcium Brine at High Temperatures with Adsorbed Sulfonated Copolymers. *Langmuir* **2013**, *29* (10), 3195−3206.

(52) Hadia, N. J.; Ng, Y. H.; Stubbs, L. P.; Torsæter, O. High salinity and high temperature stable colloidal silica nanoparticles with wettability alteration ability for eor applications. *Nanomaterials* **2021**, *11* (3), 707.

(53) Bradford, S. A.; Kim, H.; Shen, C.; Sasidharan, S.; Shang, J. Contributions of Nanoscale Roughness to Anomalous Colloid Retention and Stability Behavior. *Langmuir* **2017**, *33* (38), 10094−10105.

(54) Zou, Y.; Jayasuriya, S.; Manke, C. W.; Mao, G. Influence of Nanoscale Surface Roughness on Colloidal Force Measurements. *Langmuir* **2015**, *31* (38), 10341−10350.

(55) Zeng, Y.; Qian, H.; Chen, X.; Li, Z.; Yu, S.; Xiao, X. Thermodynamic Estimate of PKa Values of the Carboxylic Acids in Aqueous Solution with the Density Functional Theory. *Chin. J. Chem.* **2010**, *28* (5), 727−733.

(56) Marinova, K. G.; Alargova, R. G.; Denkov, N. D.; Velev, O. D.; Petsev, D. N.; Ivanov, I. B.; Borwankar, R. P. Charging of Oil−Water Interfaces Due to Spontaneous Adsorption of Hydroxyl Ions. *Langmuir* **1996**, *12* (8), 2045−2051.

(57) Kutuzov, S.; He, J.; Tangirala, R.; Emrick, T.; Russell, T. P.; Böker, A. On the Kinetics of Nanoparticle Self-Assembly at Liquid/Liquid Interfaces. *Phys. Chem. Chem. Phys.* **2007**, *9* (48), 6351−6358.

(58) Reincke, F.; Kegel, W. K.; Zhang, H.; Nolte, M.; Wang, D.; Vanmaekelbergh, D.; Möhwald, H. Understanding the Self-Assembly of Charged Nanoparticles at the Water/Oil Interface. *Phys. Chem. Chem. Phys.* **2006**, *8* (33), 3828−3835.

(59) Liu, F.; Tang, C.-H. Emulsifying Properties of Soy Protein Nanoparticles: Influence of the Protein Concentration and/or Emulsification Process. *J. Agric. Food Chem.* **2014**, *62* (12), 2644−2654.

(60) Du, K.; Glogowski, E.; Emrick, T.; Russell, T. P.; Dinsmore, A. D. Adsorption Energy of Nano- and Microparticles at Liquid−Liquid Interfaces. *Langmuir* **2010**, *26* (15), 12518−12522.

(61) Liu, C.-W.; Liu, H.-S. Rhodococcus Erythropolis Strain NTU-1 Efficiently Degrades and Traps Diesel and Crude Oil in Batch and Fed-Batch Bioreactors. *Process Biochem.* **2011**, *46* (1), 202−209.

(62) Simon, S.; Subramanian, S.; Gao, B.; Sjöblom, J. Interfacial Shear Rheology of Gels Formed at the Oil/Water Interface by Tetrameric Acid and Calcium Ion: Influence of Tetrameric Acid Structure and Oil Composition. *Ind. Eng. Chem. Res.* **2015**, *54* (35), 8713−8722.

(63) Toor, A.; Forth, J.; Bochner de Araujo, S.; Merola, M. C.; Jiang, Y.; Liu, X.; Chai, Y.; Hou, H.; Ashby, P. D.; Fuller, G. G.; Russell, T. P. Mechanical Properties of Solidifying Assemblies of Nanoparticle Surfactants at the Oil−Water Interface. *Langmuir* **2019**, *35* (41), 13340−13350.

(64) Dai, L.; Bergfreund, J.; Reichert, C. L.; Fischer, P.; Weiss, J. Shear Rheological Properties of Acid Hydrolyzed Insoluble Proteins from Chlorella Protothecoides at the Oil-Water Interface. *J. Colloid Interface Sci.* **2019**, *551*, 297−304.

(65) van der Vaart, K.; Rahmani, Y.; Zargar, R.; Hu, Z.; Bonn, D.; Schall, P. Rheology of Concentrated Soft and Hard-Sphere Suspensions. *J. Rheol.* **2013**, *57* (4), 1195−1209.

(66) Pham, K. N.; Petekidis, G.; Vlassopoulos, D.; Egelhaaf, S. U.; Poon, W. C. K.; Pusey, P. N. Yielding Behavior of Repulsion- and Attraction-Dominated Colloidal Glasses. *J. Rheol.* **2008**, *52* (2), 649−676.